Nonsingular defects and self-assembly of colloidal particles in cholesteric liquid crystals

Rahul P. Trivedi, Mykola Tasinkevych, and Ivan I. Smalyukh

Phys. Rev. E **94**, 062703 — Published 14 December 2016

DOI: 10.1103/PhysRevE.94.062703

Nonsingular Defects and Self-Assembly of Colloidal Particles in Cholesteric Liquid Crystals

Rahul P. Trivedi[1,2] , Mykola Tasinkevych[3,4] and Ivan I. Smalyukh[1,2,5,6*]

[1]Department of Physics, University of Colorado, Boulder, CO 80309, USA
[2]Department of Electrical, Computer and Energy Engineering, University of Colorado, Boulder, CO 80309, USA
[3]Max-Planck-Institut für Intelligente Systeme, Heisenbergstr. 3, D-70569 Stuttgart, Germany
[4]IV. Institut für Theoretische Physik, Universität Stuttgart, Pfaffenwaldring 57, D-70569 Stuttgart, Germany
[5]Soft Materials Research Center and Materials Science and Engineering Program, University of Colorado, Boulder, CO 80309, USA
[6]Renewable and Sustainable Energy Institute, National Renewable Energy Laboratory and University of Colorado, Boulder, CO 80309, USA

*E-mail: ivan.smalyukh@colorado.edu

Abstract. Cholesteric liquid crystals can potentially provide a means for tunable self-organization of colloidal particles. However, the structures of particle-induced defects and the ensuing elasticity-mediated colloidal interactions in these media remain much less explored and understood as compared to their nematic liquid crystal counterparts. Here we demonstrate how colloidal microspheres of varying diameter relative to the helicoidal pitch can induce dipole-like director field configurations in cholesteric liquid crystals, where these particles are accompanied by point defects and a diverse variety of nonsingular line defects forming closed loops. Using laser tweezers and nonlinear optical microscopy, we characterize the ensuing medium-mediated elastic interactions and three-dimensional colloidal assemblies. Experimental findings show a good agreement with numerical modeling based on minimization of the Landau-de Gennes free energy and promise both practical applications in the realization of colloidal composite materials and means of controlling nonsingular topological defects that attract a great deal of fundamental interest.

1. Introduction

Foreign particles introduced into nematic liquid crystals (LCs) typically prompt formation of defects in their vicinity in order to compensate for the boundary conditions at the particle surfaces, such that the net topological hedgehog charge of the system is conserved [1,2]. The nature of defects and resultant symmetries in the particle-induced deformations of the director field depend on the type and strength of surface anchoring [1-6] and also on the shape and topology of the particles [7-18]. For example, particles with strong homeotropic surface anchoring give rise to hyperbolic hedgehog point defects, imparting dipolar symmetry to the resultant director configuration [1]. Particles with weak homeotropic anchoring (or having size comparable to the cell thickness) give rise to half-integer disclination loops (also called a "Saturn-ring" defect) around them and the resulting elastic quadrupolar symmetry [2-4]. Similar types of dipolar and quadrupolar symmetries of elastic deformations in the LCs were also demonstrated for particles with tangential and other boundary conditions for the nematic director [19-27]. Nematic colloids with hexadecapolar symmetry of elastic distortions have been recently observed too [28]. The particle-induced defects stabilized by the colloidal particles and the resultant deformation in $\mathbf{n}(\mathbf{r})$, lead to new kinds of elasticity-mediated colloidal interactions in nematic LCs [1], which, in turn, give rise to one- two- and three-dimensional colloidal structures, such as chains and crystal arrays [29].

Colloidal interactions involving the orientational elasticity effects have been studied in depth and well-understood for nematic LCs but the case of cholesteric LCs remains much less explored [30-45]. It can be heuristically argued that, because of the periodic helicoidal structure, cholesteric LCs promise a richer landscape for formation of defects around colloidal particles and resultant interactions between them, as compared to the case of

nematic LCs [30-45]. Furthermore, the parameter d/p (ratio of diameter of the particle to the intrinsic pitch of the cholesteric LC) can be potentially exploited to "tune" the nature of defects and the ensuing elastic interactions. For example, a particle with $d << p$ is expected to effectively "see" the local cholesteric medium as a weakly twisted "nematic", but a very different behavior can be expected in the regime of $d \geq p$. Indeed, recent studies (both experimental and theoretical) of colloidal particles with sizes comparable or larger than the cholesteric pitch revealed a large variety of singular defect loops that match surface boundary conditions at particle-LC interfaces to the far-field uniformly twisting helicoidal structure of the cholesteric LC [31,38,39]. However, these studies of colloidal dispersions typically dealt with singular loops of defect lines and revealed only a subset of possible field configurations.

In this work, we demonstrate how colloidal spheres with perpendicular (homeotropic) surface boundary conditions for the director field $\mathbf{n}(\mathbf{r})$ and with varying diameter relative to the helicoidal pitch can induce dipole-like director field configurations in cholesteric LCs. We show that these particles are accompanied by singular point defects and different types of nonsingular line defects. Using laser tweezers [41,46,47] and nonlinear optical microscopy [48], we characterize the elasticity-mediated colloidal interactions and the ensuing three-dimensional (3D) colloidal assemblies. We study how various kinds of elasticity- and defect-mediated interactions lead to 3D assemblies of colloidal particles bound by elastic forces or by entangled defects. The experiments show a good agreement with numerical modeling based on the minimization of the Landau-de Gennes free energy [49,50]. Our findings may provide the means of generating and controlling nonsingular topological defect lines and their loops as well as could lead to

novel approaches for the design and realization of LC-colloidal composite materials with pre-engineered properties and response to external stimuli like electric fields [51-54].

2. Experimental methods, technique, and materials

Cholesteric LCs are prepared by mixing the room-temperature nematic hosts 4-Cyano-4'-pentylbiphenyl (5CB) or ZLI2806 with a chiral dopant CB15 (all from EM Chemicals). The helicoidal pitch p value is set by controlling the volume fraction of the chiral additive (C_{chiral}) of known helical twisting power for a given nematic host h_{HTP} [30] according to the relation $p = (h_{HTP} \times C_{chiral})^{-1}$, which works well for relatively small volume fractions of the chiral additive ~0.01 used in this study [30,45]. For the mixtures obtained by doping CB15 into the 5CB nematic host, h_{HTP}=7.3 μm^{-1}, whereas h_{HTP}=5.9 μm^{-1} for the cholesteric mixtures prepared by doping CB15 into the ZLI2806 nematic host [30]. These h_{HTP} values were used to calculate C_{chiral} for the values of pitch in the range p=5-25 μm, as presented for particular experiments in the captions of the corresponding figures. Additionally, the values of p where measured separately using the Grandjean-Cano method [30,44-46], showing a good agreement with the values estimated based on the chiral additive volume fractions during the LC sample preparation. We have utilized solid silica particles of known nominal diameter [18]. These particles were treated with N,N-dimethyl-N-octadecyl-3-aminopropyl-trimethoxysilyl chloride (DMOAP), by following procedures detailed elsewhere [8,18], in order to set perpendicular surface boundary conditions for the LC director on the colloidal particle surfaces. The particles were re-dispersed in the LC and the resultant dispersion was then sonicated to break occasional particle aggregates. LC cells were fabricated using two glass substrates of thickness 0.15 *mm*, as required for the optimization of imaging and optical trapping with high numerical aperture (1.4) oil immersion objectives. Strong planar

surface anchoring boundary conditions on the inner surfaces of confining substrates of the cells were set by spin-coating and curing a thin layer of polyimide PI-2555 (HD Micro-Systems), and then unidirectionally rubbing it with a piece of velvet cloth to define the surface boundary conditions for the LC director. The thickness of LC cells was set within 30-60 μm by sandwiching the glass substrates with silica microspheres of corresponding diameters and (based on the 3D nonlinear optical imaging of the vertical cross-sections described below) was found to be uniform, with variations smaller than 1μm [8,11,21]. The substrates were glued together using fast-setting epoxy [42,43]. The colloidal dispersions in the cholesteric LC were infiltrated into the cells by using capillary forces.

Optical manipulation and 3D imaging were performed with an integrated setup composed of holographic optical tweezers and a multimodal nonlinear optical imaging system described in details elsewhere [46,48]. The 3D director structures were studied using a combination of conventional polarizing optical microscopy and a 3D nonlinear imaging technique dubbed "three-photon excitation fluorescence polarizing microscopy" (3PEF-PM) [48], which is based on fluorescence of the cholesteric LC (including the chiral additive) molecules excited through three-photon absorption of femtosecond infrared laser light. The 3PEF-PM fluorescence intensity exhibits a strong dependence on the orientation of linear polarization of the excitation beam relative to $\mathbf{n}(\mathbf{r})$ [48]. 3PEF-PM images were comprised of 3D stacks of optical slices and were used to reveal director structures as well as relative positions of colloidal particles, and the corresponding locations and configurations of topological defects accompanying them. All presented optical microscopy observations, as well as the laser trapping and 3D imaging experiments were performed using a 100× or 60× oil immersion objectives with numerical aperture ≈1.4. Optical video microscopy allowed us to probe colloidal particle dynamics through recording the particle

motion with a charge coupled device camera (Flea, PointGrey) or a fast camera HotShot 512SC (from NAC Image Technology, Inc.). We then determined the time-dependent spatial positions of the particles from captured image sequences using motion tracking software ImageJ (freeware obtained from the National Institute of Health), which was then used to estimate the particle velocities, interaction potentials and forces [28], as discussed in details elsewhere [7,12].

3. Diversity of cholesteric LC defects induced by colloidal particles

Experiments and theoretical modeling of cholesteric LC colloids conducted thus far have typically revealed twisted Saturn-ring types of defects around particles with homeotropic surface anchoring [32-47]. The disclination loop commonly winds around the particle due to the inherent helicoidal structure of the cholesteric LC's ground-state director field. In this work, in addition to the twisted disclination loop defects, we report observation of point defect in the vicinity of spherical colloidal microparticles, albeit these defect-colloidal elastic "dipoles" are significantly different from their nematic counterparts (Fig. 1). We experimentally confirm the existence of long-term stable point defects as shown in Fig. 1, where we use a high-power (~250mW) optical trap to locally melt the cholesteric LC with ≈12 μm pitch in a small region surrounding a particle of 10 μm diameter. Upon turning off the laser trap, the locally melted LC quenches back to cholesteric phase and at first exhibits a singular twisted disclination loop (Fig. 1). However, this singular disclination loop, which is clearly visible because of strong light scattering, relaxes over a time period of 5-10 s to a point defect as shown using the image sequences in Fig. 1(a,d). The resultant point defect can be seen in an image taken between crossed polarizers, Fig. 1(b,e), as well. Interestingly, bright field and dark field optical microscopy observations and

light scattering reveal no additional singular defects. The deformation of **n**(**r**) in the vertical plane (orthogonal to cholesteric helicoidal pseudo-layers reflecting the periodicity of director twist) can be seen in vertical 3PEF cross-section shown in Fig. 1(c). The sequence of micrographs shown in Fig. 1(d) reveals a similar transformation of a twisted singular disclination loop to a point defect when a particle of the same 10 μm diameter is studied within the cholesteric LC of longer pitch (≈25 μm), with the vertical cross-section of the helicoidal pseudo-layered structure shown in Fig. 1(f).

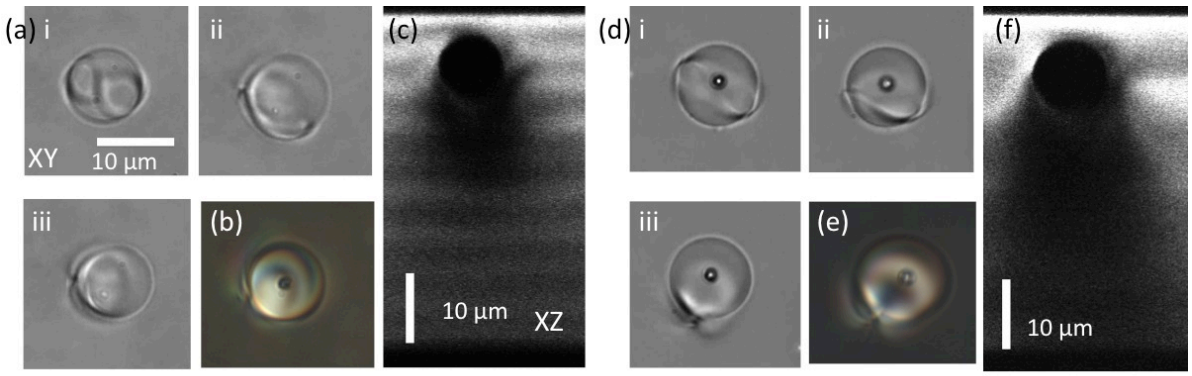

Fig. 1. Optical imaging of defects around a spherical colloidal particle in a cholesteric LC. (a) After the LC around a particle is locally melted using optical tweezers, upon quenching, a twisted singular disclination loop appears (i) and then continuously transforms (ii,iii) transforms into a point defect, which can be seen from the bright field micrograph based on scattering (iii). The 10-μm diameter spherical particle in (a-c) is studied in medium of a p=12μm cholesteric LC. (b) Observation of the particle and the induced point defect in the polarizing optical micrograph obtained between crossed polarizers parallel to the micrograph's edges. (c) 3PEF-PM vertical cross-section of the helicoidal pseudo-layered structure of the cholesteric LC around the particle. (d-f) A set of images similar to the ones shown in (a-c), respectively, but for a particle 10 μm in diameter incorporated into a cholesteric LC with the p=25 μm pitch.

The observed transformation of a disclination loop into a point defect appears to be qualitatively similar to that known for nematic LCs, where point defects have lower free energy and are more stable than the ring-shaped disclination loops for colloidal microparticles with strong homeotropic anchoring dispersed in thick LC cells [1,56,57]. Indeed, what distinguishes our experiments as compared to the previous experimental

studies [31] is that the particles are placed in cells much thicker than the particle diameter [33], as well as that the particle size is relatively large. However, the 3PF-PM cross-sectional images shown in Fig. 1(c,f) reveal that the cholesteric pseudo-layers (each corresponding to π-twist of the director) are actually interrupted by the particles, as well as that the director field configuration is much more complex as compared to that observed for the defect-colloidal dipoles in nematics [1,18]. Therefore, we use numerical modeling to gain insights into the structure of the director field configurations in these cholesteric LC colloids, as discussed below.

4. Theoretical determination of particle-induced field configurations

4.1 Landau-de Gennes Free Energy and Surface Anchoring Energy Terms

Within the framework of Landau-de Gennes (LdG) theory, LCs are described by a traceless symmetric tensor order parameter (OP) $Q_{ij}, i, j = 1,..,3$, which may be related to the anisotropic (deviatoric) part of the magnetic susceptibility tensor of the liquid crystalline material [55]. By definition $Q_{ij} = 0$ in the isotropic phase and different from zero in orientationally ordered nematic or cholesteric phases. According to the Landau phenomenological approach, the Landau-de Gennes free energy density is presented as a Taylor expansion in the scalar combinations of the tensor OP: Tr$\mathbf{Q}^2$ and Tr$\mathbf{Q}^3$, where Tr indicates a trace operator. Usually, the expansion series is truncated to the forth power in Q_{ij} without losing the physics of the nematic-isotropic phase transition, but in general, higher order terms are present. Then, to the forth order in Q_{ij}**,** the general form of the Landau-de Gennes free energy functional F_{LdG} of a chiral nematic may be written as [55,56]:

$F_{LdG} =$

$$\int_V \left(aQ_{ij}^2 - bQ_{ij}Q_{jk}Q_{ki} + c\left(Q_{ij}^2\right)^2 + \frac{L_1}{2}\partial_k Q_{ij}\partial_k Q_{ij} + \frac{L_2}{2}\partial_j Q_{ij}\partial_k Q_{ik} + \frac{4\pi L_1}{p}\varepsilon_{ijk}Q_{il}\partial_j Q_{kl} \right) dV, \quad (1)$$

where p is the equilibrium cholesteric pitch and summation over repeated indices is assumed. The phenomenological expansion coefficients a, b, and c are in the general case functions of temperature T. In practice, a is assumed to depend linearly on T, while b, and c are considered temperature independent. The nematic-isotropic phase transition is controlled by the T-dependent coefficient a, which is taken to be in the form $a(T) = a_0(T - T^*)$, where a_0 is a material dependent constant and T^* is the supercooling limit temperature of the isotropic phase. The phenomenological parameters L_1, and L_2 can be related to the Frank-Oseen splay, K_{11}, twist, K_{22}, and bend, K_{33}, elastic constants. To this end one must substitute into Eq. (1) an uniaxial *Ansatz* $Q_{ij} = \frac{3Q_b}{2}(n_i n_j - \frac{\delta_{ij}}{3})$, where Q_b is the bulk value of the scalar orientational order parameter, and n_i are the Cartesian components of the director field, and transform the gradient terms to the standard Frank-Oseen splay, twist and bend elastic free energy densities. This gives $K_{11} = K_{33} = 9Q_b^2(L_1 + L_2/2)/2$, and $K_{22} = 9Q_b^2 L_1/2$. In general K_{11} and K_{33} are diffeerent, but in most cases the difference is small and the LdG free energy (1) provides an adequate description. In general, additional (also higher order) gradient terms in the free energy expansion (1) are possible, which will make the corresponding K_{11} and K_{33} to be different from each other. However, the introduction of higher order gradient terms will not change the physical picture, and therefore here we restrict our attention only to the minimalistic model where K_{11} and K_{33} are equal to each other (which is actually the case for the experimental material parameters of ZLI2806, for which $K_{11} \approx K_{33}$ [30]), but different from

K_{22}. The integral in Eq. (1) is taken over the three-dimensional domain V occupied by the LC with the immersed colloidal particles.

We describe homeoptropic (perpendicular) anchoring of the director at the surface of colloidal particle by the following surface anchoring free energy functional

$$F_s = W \int_{\partial V} \left(Q_{ij} - Q_{ij}^s\right)^2 ds, \quad (2)$$

where $W > 0$ is the anchoring strength, and the surface-preferred value of the tensor order parameter $Q_{ij}^s = 3Q_b(N_iN_j - \delta_{ij}/3)/2$, where $\mathbf{N}$ is the normalized outward normal vector to the confining surface and δ_{ij} is the Kronecker delta symbol.

The uniaxial nematic with the bulk order parameter $Q_b = b/8c\,(a + \sqrt{1 - 8\tau/9})$ is thermodynamically stable at $\tau \equiv 24ac/b^2 < 1$. We use $a_0 = 0.044\times10^6 J/m^3$, $b = 0.816\times10^6 J/m^3$, $c = 0.45\times10^6 J/m^3$, $L_1 = 6\times10^{12} J/m,$, and $L_2 = 12\times10^{12} J/m$, which are typical values for 5CB [57] and $T^* = 307\ K$. For these values of the model parameters, the bulk correlation length $\xi = 2\sqrt{2}c(3L_1 + 2L_2)/b \cong 15nm$ at the isotropic-nematic coexistence and at $\tau = 1$ [58].

4.2 Geometry and Initial Conditions for Computer Simulations

We consider the sample volume $V = L\times L\times L$ and assume that the colloidal particle of radius R=$d/2$ has its center $\mathbf{r}_c = (0,0,0)$ in the center of the computational cube. As the initial conditions we use a combination of an uniaxial twisted equilibrium configuration (at far distances from the colloidal particle), isotropic configuration (within a spherical shell, with the outer radius R_i, around the particle) and the dipole *Ansatz* of Lubensky et al. [59] (applied within a spherical shell with the outer radius $R_h < R_i$ around the particle) to model a hedgehog defect. Thus, at a point $\mathbf{r}$ which satisfies $\| \mathbf{r} - \mathbf{r}_c \| > R_i$ we set the initial

nematic director $\mathbf{n}_0 = (-\sin(q_0(L/2-y)), 0, \cos(q_0(L/2-y)))$, with the initial degree of the nematic orientational order $Q_0 = Q_b$, where $q_0 = 2\pi/p$ and for $R_h < \| \mathbf{r} - \mathbf{r}_c \| \leq R_i$ we set $Q_0 = 0$. Next, in the domain $R \leq \| \mathbf{r} - \mathbf{r}_c \| \leq R_h$ we set

$$\mathbf{n}_0 = (\sin\Theta(\mathbf{r})\cos\phi, \sin\Theta(\mathbf{r})\sin\phi, \cos\Theta(\mathbf{r})), \quad (3)$$

where ϕ is the azimuthal angle and the director tilt angle [59]

$$\Theta(\mathbf{r}) = 2\theta - \operatorname{atan}\frac{r\sin\theta}{r\cos\theta + z_d} - \operatorname{atan}\frac{z_d r\sin\theta}{z_d r\cos\theta + 1}. \quad (4)$$

In Eq. (4) $r = ||\mathbf{r}||$, θ is the polar angle, and z_d is the $z-$coordinate of the hyperbolic hedgehog. The Lubensky *Ansatz* in Eq. (3) is constructed by using the solution $\mathbf{n}_{2D} = (\sin\Theta(\mathbf{r}_{2D}), \cos\Theta(\mathbf{r}_{2D}))$ to the corresponding two-dimensional problem and then spinning it (the solution) about the z axis to give Eq. (3). In the corresponding two-dimensional system $\Theta(\mathbf{r}_{2D})$ describes the superposition of three topological defect: the original hedgehog defect of the strength $q = -1$ at $(0, -z_d)$; and two compensating defects needed to satisfy the normal boundary conditions at the surface of the colloids, one defect with $q = +2$ placed at (0,0), and another with $q = -1$ at $(0, -z_d^{-1})$. The last defect is an image of the original hedgehog. One example of such initial configuration is illustrated in Fig. 2. Finally, we always set $L = np$, where n is an integer, and impose fixed boundary conditions on Q_{ij} with the values specified by the expression on Q_{ij}^0 evaluated at the system boundaries ∂V.

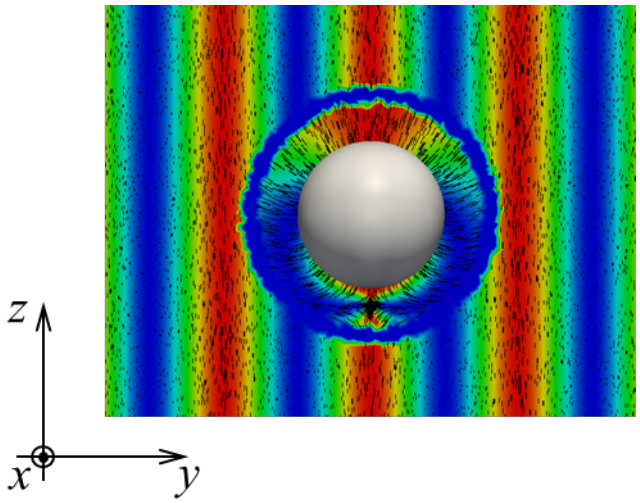

Fig. 2. An example of the initial configuration used to initialize the numerical minimization of the total free energy given by Eq.(1) plus Eq.(2) with $R_i = 1.75R, R_h = 1.5R$ (see text for details), and cholesteric pitch $p = 4R = 2d$. The color scale encodes n_z^2, where n_z is the component of the director perpendicular to the far-field helical axis χ and along the vertical edge of the computer-simulated presentations of the 3D director configurations, such as the initial conditions shown here; in the color scheme encoding n_z, red corresponds to n_z^2 =1, blue to n_z^2 =0, and all other colors to the values within 0-1. In the initial configuration, the nematic dipole ansatz within the volume separated by the inner sphere and the ground-state cholesteric helicoidal structure far away from the particle down to the outer sphere are separated by an isotropic region (blue) in-between the two spheres. Spatially varying orientations of the black rods represent the director field.

4.3 Details and Procedures of Numerical Modeling

In the following, the Landau-de Genens free energy Eq. (1), augmented by the surface term in Eq. (2), is minimized numerically using finite elements method with the adaptive mesh

refinement. The surface of colloidal particle is represented by a union of triangles using open source GNU Triangulated Surface Library [60], and then the nematic-containing domain of the sample with the volume V is discretized by using the Quality Tetrahedral Mesh Generator [61]. Linear triangular and tetrahedral elements are used and the integration over the elements is performed numerically by using fully symmetric Gaussian quadrature rules [62-64]. Consequently, the discretized F_{LdG} is minimized exploiting INRIA's M1QN3 optimization routine [65]. A more detailed description of the numerical simulation procedures is provided in Ref. [66].

4.4 Results of Numerical Modeling

Figures 3-5 summarize the numerically calculated LC configurations for the values of the equilibrium cholesteric pitch, $p = 4R, 3R, 2R$, respectively. In all three cases we observe the formation of a hedgehog "point" defect nearby the colloidal particle, consistent with the experiments (Fig. 1). The point defects are located in the plane passing through the equatorial midplane of the colloidal sphere parallel to the cholesteric "pseudo-layers", which, in turn, are orthogonal to the far-field helical axis χ. The core of the hyperbolic hedgehog point defect has the fine structure of a half-integer disclination ring [67-71], Figs. 3(b), 4(b), and 5(b), with the radius of the tube forming a torus-shaped region of reduced order parameter in the range of few nematic coherence lengths ξ. The observation of such ring-shaped core of a point defect is consistent with theoretical models [68-71] and recent experiments [67]. The point defects are found localizing along an axis passing through the microsphere center perpendicular to the far-field helicoidal axis and parallel to the far-field helicoidal director orientation at the sample depth location of the particle's center.

The planes containing the singular disclination rings are oriented perpendicular to the $z-$axis and parallel to the local surface of the near-by colloidal microsphere for all studied values of p, Figs. 3(b), 4(b), and 5(b). These point defects with the ring-like structure of the core are the only singular defects induced by the nematic colloidal particles with perpendicular anchoring in the cholesteric LC. However, we also observe the non-singular solitonic configurations shown in Figs. 3,4.5(c,d) by the green surfaces. These solitonic nonsingular configurations are comprised of closed loops of the so-called $\lambda-$lines and are characterized by the escape of the director into the 3rd dimension, which in our case is the direction along the solitonic line's contour [Figs. 3(d), 4(d), and 5 (d)]. Surprisingly, the scalar order parameter around the $\lambda-$lines has values slightly larger than the corresponding bulk values, which allows to visualize the twist-escaped cores of the defect lines based on the increased local value of the scalar order parameter [Figs. 3(d), 4(d), and 5(d)], in contrast to the singular defects that have locally decreased values of the scalar order parameter within their cores [Figs. 3(b),4(b) and 5(b)]. Since the director field within the loops of nonsingular defect lines is continuous, these solitonics structures are not expected to cause light scattering and (unlike the singular defects) are thus "invisible" in bright-field micrographs, in agreement with the experimental observations (Fig. 1).

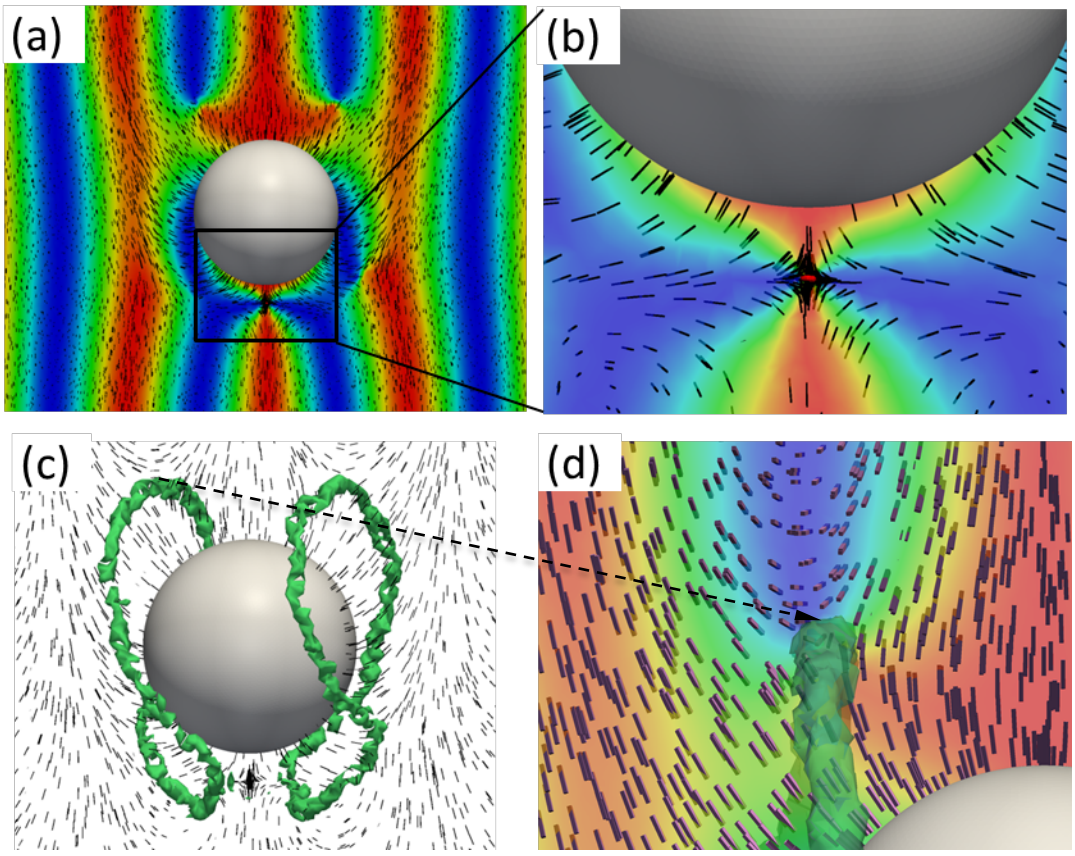

Fig. 3. LC configurations at $p = 4R, R = 1\mu m$ shown (a) with the help of a cross-section passing through the particle center and the hyperbolic point defect nearby and (b) within a zoomed-in region of this cross-section in the vicinity of a point defect; (c) as a three-dimensional perspective view of the nonsingular solitonic structure and the director field cross-section shown in (a), with the zoomed-in region showing details of the nonsingular twist-escaped configuration depicted in (d). We note that the 3D perspective view in (c), unlike the individual cross-section in (a), shows 3D perspective presentations of the molecular rods and director when they are in all possible orientations, including the ones orthogonal to the cross-sectional image plane. In (a,b,d) color encodes n_z^2, where n_z is the vertical (in the frame of the figure) component of the director; red color corresponds to n_z^2 =1, blue to n_z^2 =0, and the other colors to the values within 0-1. In (b) the split-core structure of the hyperbolic hedgehog is shown as an iso-surface (a small red ring, viewed edge-on and perpendicular to the plane of the figure) corresponding to a constant value $Q < Q_b$ of the scalar orientational order parameter. The green surfaces in (c,d) correspond to the iso-surfaces of a constant $Q > Q_b$ and represent non-singular defect lines, the so-called λ −lines. Spatially varying orientations of the black rods represent the director field.

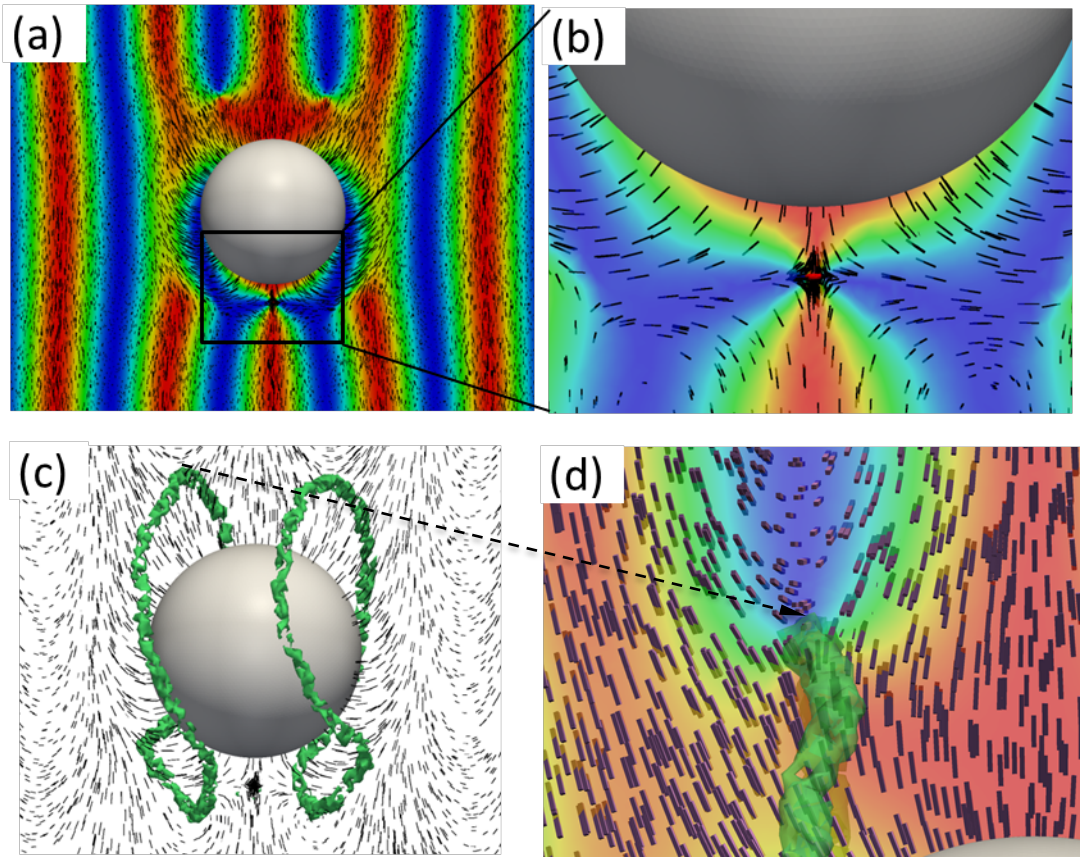

Fig. 4. LC configurations at $p = 3R$, $R = 1\mu m$ shown (a) with the help of a cross-section passing through the particle center and the hyperbolic point defect nearby and (b) within a zoomed-in region of this cross-section in the vicinity of a point defect. (c) A three-dimensional perspective view of the nonsingular solitonic structure and the director field cross-section shown in (a), with the zoomed-in region showing details of the nonsingular twist-escaped configuration depicted in (d). In (a,b,d), the colors encode n_z^2, where n_z is the vertical (in the frame of the figure) component of the director; red color corresponds to n_z^2 =1, blue to n_z^2 =0, and the other colors to the values of n_z^2 within 0-1. In (b) the split-core structure of the hyperbolic hedgehog is shown as an iso-surface (a small red ring, viewed edge-on and perpendicular to the plane of the figure) corresponding to a constant value $Q < Q_b$ of the scalar orientational order parameter. The green surfaces in (c,d) correspond to the iso-surfaces of a constant $Q > Q_b$ and represent non-singular $\lambda-$defect lines. Spatially varying orientations of the black rods represent the director field.

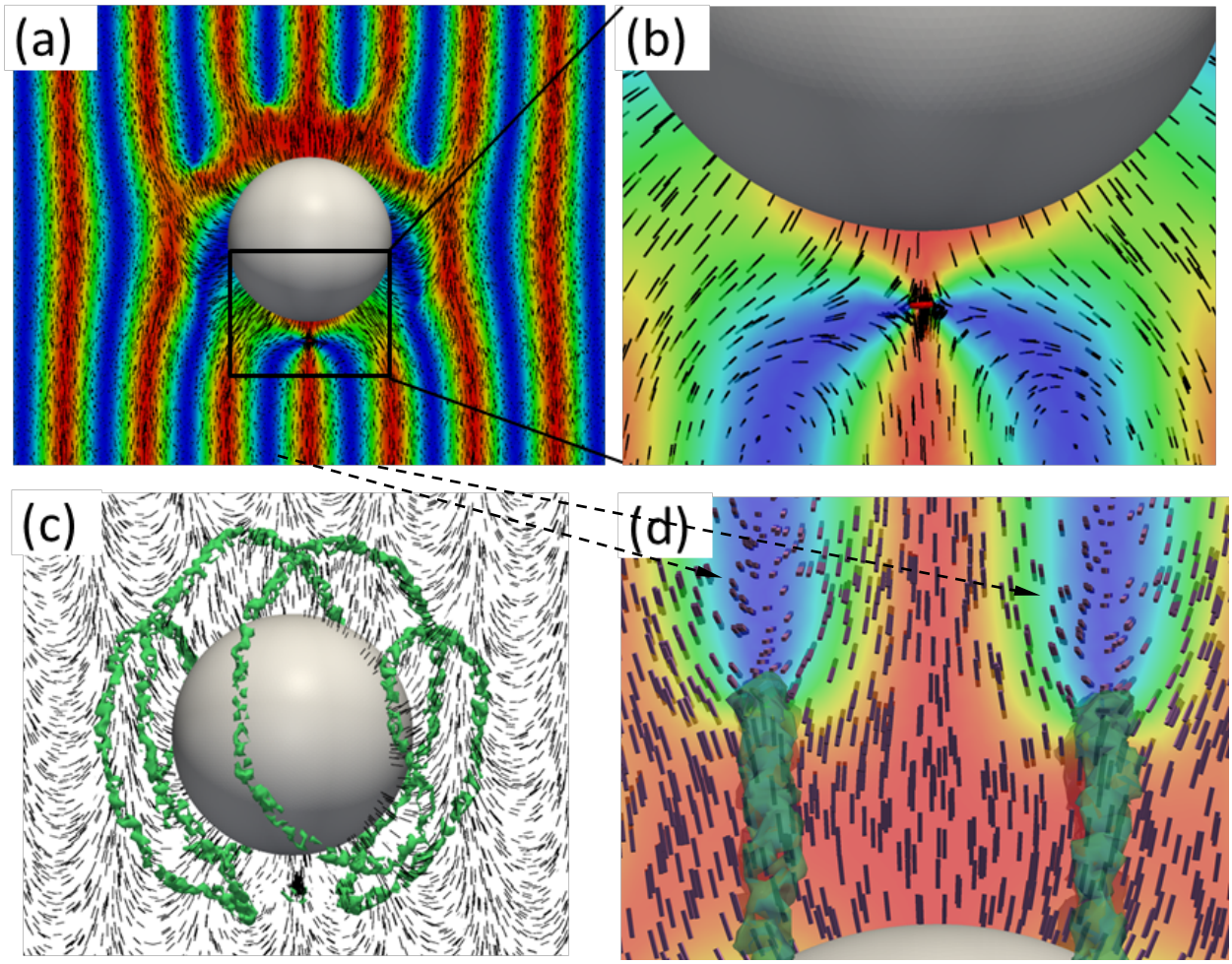

Fig. 5. LC configurations at $p = 2R$ shown (a) with the help of a cross-section passing through the particle center and the hyperbolic point defect nearby and (b) within a zoomed-in region of this cross-section in the vicinity of a point defect. (c) A three-dimensional perspective view of a nonsingular solitonic structure and the director field cross-section shown in (a), with the zoomed in region depicted in (d) showing details of the nonsingular twist-escaped configuration. In (a,b,d), the colors encode n_z^2, where n_z is the vertical (in the frame of the figure) component of the director; red color corresponds to n_z^2 =1, blue to n_z^2 =0, and the other colors to the values of n_z^2 within 0-1. In (b) the split-core structure of the hyperbolic hedgehog is shown with the help of an iso-surface (a small red ring, viewed edge-on and perpendicular to the plane of the figure) corresponding to a constant value $Q < Q_b$ of the scalar orientational order parameter. Green surfaces in (c,d) correspond to the iso-surfaces of a constant $Q > Q_b$ and represent non-singular (in the material director field) defect lines with twist-escaped defect cores, the so-called λ −lines [30,41]. Spatially varying orientations of the black rods represent the director field.

5. Colloidal self-assemblies

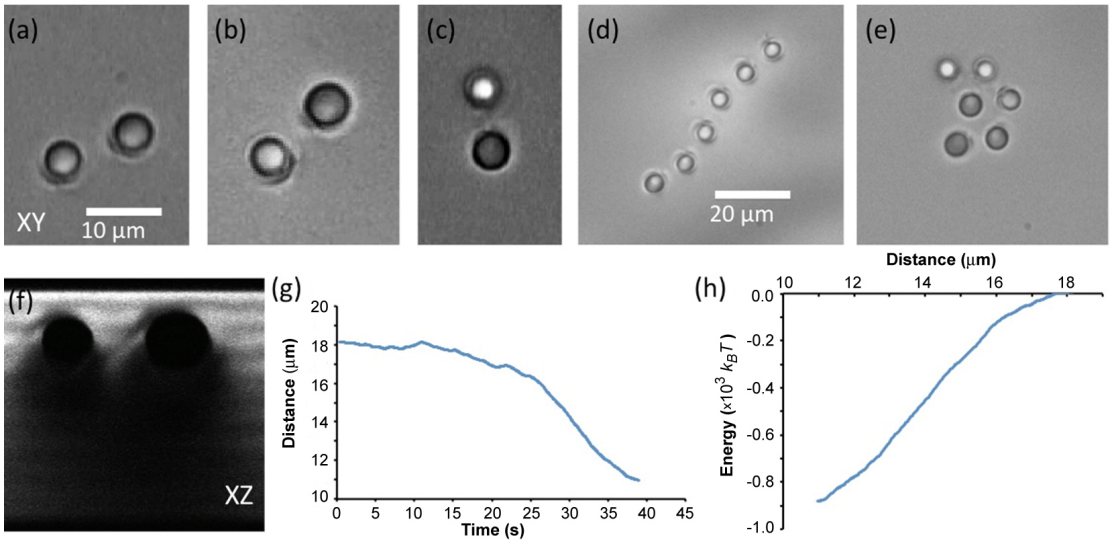

Fig. 6. Elastically bound colloidal particle assemblies. (a-c) Chiral dipolar particles form assemblies prompted by attractive elastic interactions. These assemblies are not only confined to the same cholesteric pseudo-layer as in (a,f) but also form when the particles are separated along the helical axis by ≈p/4 (b) or ≈p/2 (c). We note that these are just examples and other initial center-to-center inter-particle separations are possible too, albeit particle interactions become weak at separations >p. (d) An in-plane assembly of multiple chiral dipolar particles, with the configuration of a curved chain. (e) An assembly formed by several particles at different depths along the helical axis. (f) Two particles confined to the same cholesteric pseudo-layer shown in the vertical cross-section image obtained by using 3PEF-PM and corresponding to (a). (g) Inter-particle separation as a function of time, probed while the particles are attracted towards each other to form the in-plane assembly in (a). (h) The interaction energy of the assembly in (a) as a function of inter-particle separation.

In relatively dilute particle dispersions, we observe colloidal self-organization of microspheres in cholesteric LCs, which we explore with the help of holographic laser tweezers [46]. As shown in three exemplary scenarios in Fig. 6 (a-c), differing from nematic dipolar colloids, we observe multiple possible particle-defect end-configurations of the colloidal particles in cholesteric LCs, depending on whether the interacting particles are initially confined in the same cholesteric pseudo-layer or separated by a distance of up to $p/2$ along the helical axis. To demonstrate this, we have used d=4 μm silica particles

(treated to give homeotropic anchoring) dispersed in a p=5 μm cholesteric LC. The self-assembled elastically bound pairs of particles have center-to-center inter-particle separations ≈ 4.75R. By using laser tweezers and video microscopy, we experimentally observed that there is a strong inter-particle repulsion when colloidal inclusions are pushed towards each other with the laser tweezers. As the particle depth positions are varied using optical traps, the center-to-center separation vectors $\mathbf{r}_{d\text{-}p}$ connecting the point defect and the particle rotate synchronously with the rotation of the local director in the midplane of the microspheres (Figs. 3-5). Unlike the elastic dipoles in nematic colloids [1], which only form self-assemblies of parallel dipoles separated along the far-field director or anti-parallel dipoles separated in a direction perpendicular to the far-field director, the variety of stable and metastable two-particle self-assemblies in cholesteric LCs is enriched by the alignment of the particle-defect vectors with respect to the far-field helicoidal structure. Rather than binding only into configurations with parallel or anti-parallel orientations of the particle-defect vectors, as in nematics, cholesteric colloids can form long-term stable assemblies with these vectors' relative orientations dependent on the relative depths of their positions with respect to the surrounding far-field helicoidal structure. In-plane elasticity-mediated colloidal interaction between particles initially located at the same depths result in curved chain-like structures, i.e., the tangent to the chain contour and the direction of a participant dipole do not coincide, as shown in Fig. 6(a) and Fig. 6(d). We show the same structure in Fig. 6(f) in the cross-sectional image in the vertical xz-plane obtained using 3PEF-PM, which reveals the distortions of the cholesteric helicoidal structure locally caused by the particles. Figure 6(g) shows the inter-particle center-to-center distance as a function of time, as the particles separated apart by laser tweezers attract towards each other. Figure 6(h) shows the pair interaction energy (in the units of

k_BT, where T is the absolute temperature and k_B is the Boltzmann constant) of this pair as a function of their separation, which we derived from the experimental data shown in Fig. 6(g) by assuming that the inertia effects can be neglected and that the elastic interaction forces are balanced by the viscous drag forces [30]. We see that the magnitude of the elastic binding energy of the final two-particle colloidal configuration is about ~$800k_BT$, and hence it is very stable with respect to the effects of thermal fluctuations. This binding energy is somewhat smaller than that previously measured for nematic dipolar colloidal particles of similar size [1,21]. This observation could be related to the fact that it may be more difficult for the cholesteric LC colloids to share elastically distorted regions as compared to their nematic counterpart, thus yielding a lower elastic binding energy. The large final separation distances between particles within the self-assembled configurations can be understood from examining the computer-simulated structures shown in Figs. 3-5. Indeed, in addition to the singular point defects, our particles are separated by a coronas of perturbations of the helicoidal structure with nonsingular defect lines forming closed loops (Figs. 3-5). Bringing the particles closer would require modifying these solitonic configurations, possibly through generating additional singular defects, which is associated with strong energetic barriers that explain strong repulsive forces emerging when the particles are pushed towards each other to center-to-center distances smaller than 4R.

In Fig. 6(b,c), we demonstrate the other two possible end-configurations bound elastically to each other, where the microspheres are additionally displaced with respect to each other along the helical axis by $\approx p/4$ in Fig. 6(b) and $\approx p/2$ in Fig. 6(c). In both cases, the strengths of elasticity-mediated binding are similar to what we observed (Fig. 6) for interactions within the plane orthogonal to the far-field helical axis and within 600-$800k_BT$. By controlling the vertical positions of the particles (as the initial conditions) we can make

use of these rich elastic interactions to optically guide various colloidal assemblies, as demonstrated using two different examples shown in Fig. 6(d,e). Figure 6(d) shows an in-plane colloidal structure confined to the plane orthogonal to the far-field helical axis and akin to a curved chain formed by particles localized within the same cholesteric pseudo-layer. Figure 6(e) shows particles additionally separated along the helical axis while elastically bound to each other, forming a stable spiraling colloidal self-assembly. In concentrated dispersions of colloidal microspheres in cholesteric LCs, a large variety of combinations of these different self-assembly scenarios can be expected and, in fact, many of them have been already observed in the past experimental study of cholesteric LC colloidal emulsions [72].

In addition to the elasticity-mediated forms of self-assembly discussed above, we find that the colloidal particles can also interact with each other such that the resultant end-configurations of particles can be entangled by various loops of defect lines and with shared defect configurations that differ from that of the superposition of defect structures due to individual particles. This is an interesting class of interactions that offers multiple arrangements for optically guided 3D assembly of particles into a large zoo of desired colloidal configurations. Some of these configurations share their structural features with those observed earlier [29-41, 73], albeit loops of nonsingular defect lines are always present. The point-like defects near the particles occasionally open up to form singular disclination loops when these particles are optically pushed co-localize close to each other, which then merge into single singular defect loops entangling the colloidal pairs. In Fig. 7(a) we see two particles bound by a loop of disclination while the particle centers are displaced with respect to each other along the helical axis. This configuration is created by adjusting vertical positions of the particles and placing them with tweezers so that they attractively

interact to spontaneously form this defect configuration [Fig. 7 (d)]. Our video microscopy analysis [Fig. 7 (d) and (e)] reveals that the two-particle colloidal assembly is much more strongly bound as compared to its counterparts shown in Fig. 6, yielding the elasticity- and defect-enabled colloidal binding energy around 6,500k_BT. This binding energy is consistent with the fact that the assemblies are highly robust with respect to thermal fluctuations and always long-term stable. Once this out-of-plane, two-particle assembly is formed, it can be optically manipulated and transformed into one of the other defect-entangled particle assemblies, such as the ones shown in Fig. 7(f,g,h) and Fig. 7(i,j,k), where these new configurations are formed as a result of entanglement by different types of singular defect loops occurring in addition to nonsingular solitonic director structures.

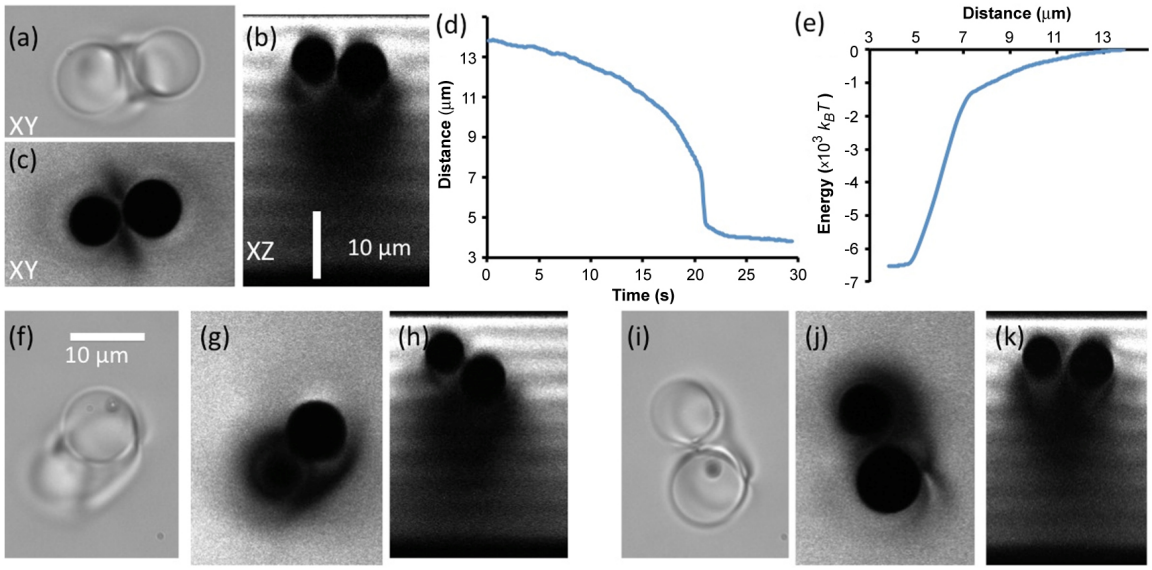

Fig. 7. Defect-bound particle assemblies studied using 10 μm diameter particles in a 12 μm pitch cholestetic LC. We optically form and switch between several types of in-plane or out-of-plane assemblies. (a,b,c) transmission micrograph (a), 3PEF-PM in-plane section (c), and 3PEF-PM vertical cross-section (b), respectively, for one type of in-plane colloidal assembly. (d) Inter-particle separation vs. time during formation of assembly shown in (f). (e) Interaction energy vs. distance between particles as it forms the colloidal assembly shown in (f). (f,g,h) similar set of images as in (a-c) but for out-of-plane defect-bound assembly. (i,j,k) Similar set of images as in (a-c) but for a different in-plane colloidal self-assembled structure.

We have also studied configurations of colloidal structures using particles with d=10 μm dispersed in a longer-pitch cholesteric LC (p≈25 μm), which are presented in Fig. 8. In this case, though, we observe a yet different kind of elasticity-mediated assembly, which is reminiscent to that leading to elastic dipolar chains in nematic LCs (Fig. 8). When particles are placed at the same depth level of the LC cell, so that their center-to-center separation vector is orthogonal to χ, the anti-parallel elastic colloidal dipoles form side-by-side assemblies shown in Fig. 8(a-d) while the parallel elastic dipoles form the end-to-end chain-like assembles following the local orientation of the director within the helicoidal structure (Fig. 8e-h). The center-to center inter-particle distances in this case are comparable to those observed for nematic colloidal dipoles [1] and much smaller relative to particle dimensions as compared to what we demonstrated in Fig. 6. This behavior is consistent with the fact that the particle diameter is $d<p/2$, making the colloidal behavior reminiscent to that of the nematic colloids [1]. Interestingly, unlike the colloidal particles in a shorter-pitch cholesteric LCs that we studied above (Figs. 6 and 7), these particles always attract to find the equilibrium structures with the final orientation of the center-to center separation vector perpendicular to χ and always in one of the two types of assemblies shown in Fig. 8, even when released from laser traps at different depths of the cell and initially separated along the cholesteric helical axis.

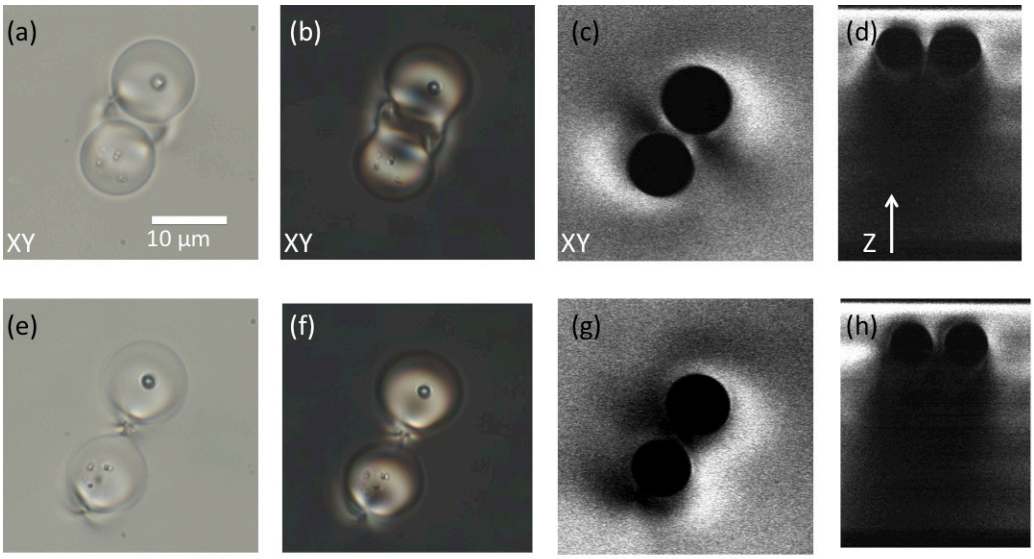

Fig. 8. Defect-bound particle assemblies of 10 μm diameter particles in a p=25μm cholesteric LC. (a-d) An in-plane colloidal assembly is shown with the help of transmission brightfield micrograph (a), polarizing optical micrograph (b), 3PEF-PM in-plane image (c), and 3PEF-PM vertical cross-section (d). (e-h) Similar set of images for a different type of colloidal particle assembly formed by parallel elastic dipoles. This configuration is similar to the linear chains formed by elastic dipolar colloidal particles in nematic LCs.

The multiple kinds of structures that we demonstrated above (both within the same cholesteric LC pseudo-layer and across the helicoidal structure) can be used as building blocks to form much larger and more complex pre-designed 3D colloidal structures. We demonstrate this designed colloidal assembly in Fig. 9, illustrating how colloidal organization can be mediated by LC elasticity and guided by laser tweezers. Figure 9(a,b) shows three- and four-particle assemblies configured in 3D into nonlinear structures, utilizing different kinds of defect-entangled and elastically bound assemblies of the constituent particles. In Fig. 9(c), we demonstrate a sequence of images illustrating step-by-step formation of a large colloidal structure spanning both along the helical axis and in the lateral plane orthogonal to it. This structure is formed using laser tweezers by bringing in and "beading" new particles to the assembly, one particle at a time, with the several stages of its formation illustrated in Fig. 9(c). Furthermore, these structures can be reconfigured

by locally melting the LC and adjusting orientations of the "bonds" between the individual colloidal inclusions.

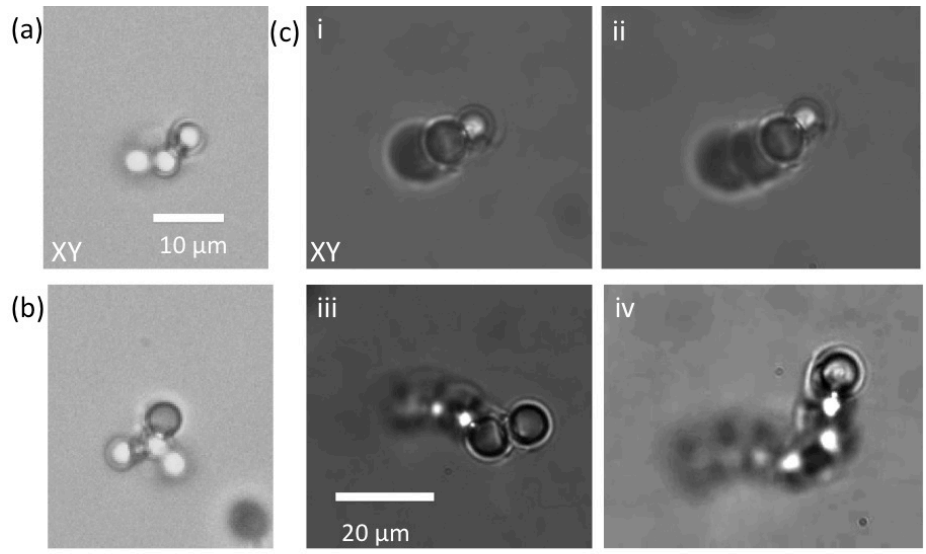

Fig. 9. 3D defect-bound multi-particle assemblies formed using d=4 μm particles dispersed in a p=5 μm cholesteric LC. (a) Optical micrographs of colloidal assemblies formed by three (a), and four particles (b). (c) A large 3D assembly formed by eight particles, created by bringing in one particle at a time, as shown with the help of selected frames at the end of the intermediate steps. The metastability of many different states within the assembly allows for reconfiguring it with the laser tweezers, so that the shape of the assembly can change continuously by shifting the particles up and down along the helix.

6. Conclusions

To conclude, we have demonstrated that the cholesteric LC hosts provide a richness of particle-induced topological defect structures (Figs. 1-5) and ensuing interactions between the colloidal inclusions (Figs. 6-9). This can be exploited to form a complex variety of two- and three-dimensional assemblies of colloidal particles with the help of optical guiding by laser tweezers (Fig. 9). The elastic potential landscape for these interactions can be tuned by varying the ratio of particle size to the pitch of the cholesteric LC (Figs. 6-8) and potentially can be further enriched by using particles with non-spherical shapes [7] and different types of surface anchoring conditions [21]. Our experimental and numerical

studies demonstrate a large variety of defect structures around spherical inclusions in cholesteric LCs and interactions between them, mediated by sharing defects and elastic deformations surrounding the particles. The type of desired assembly can be selected and guided optically with the help of laser tweezers. Since nanoparticles are known to get elastically trapped inside the hedgehog point defect and other singularities [12,18] in a nematic LC, the chiral dipolar particles and their assemblies can act as templates for 3D self-assembly of nanoparticles inside the matrix created by the micrometer-sized colloidal particles and the cholesteric LC host.

We thank P. Ackerman, T. Lee and B. Senyuk for discussions. This work was supported by the NSF grant DMR-1410735.

References:

1. P. Poulin, H. Stark, T. C. Lubensky and D. A. Weitz. Science **275**, 1770 (1997).
2. R. W. Ruhwandl and E. M. Terentjev. *Phys. Rev. E* **55**, 2958-2961 (1997).
3. Y. Gu and N. L. Abbott. *Phys. Rev. Lett*. **85**, 4719-4722 (2000).
4. S. Ramaswamy, R. Nityananda, V. A. Raghunathan, and J. Prost. *Mol. Cryst. Liq. Cryst. Sci. Technol, Sect. A* **288**, 175-180 (1996).
5. F. Brochard and P. G. de Gennes, *J. Phys. (Paris)* **31**, 691 (1970).
6. D. Andrienko, M. P. Allen, G. Skačej and S. Žumer. *Phys. Rev. E* **65**, 041702 (2002).
7. C. P. Lapointe, T. G. Mason and I. I. Smalyukh. *Science* **326**, 1083 (2009).
8. B. Senyuk, Q. Liu, S. He, R. D. Kamien, R. B. Kusner, T. C. Lubensky and I. I. Smalyukh. *Nature* **493**, 200 (2013).
9. T. A. Wood, J. S. Lintuvuori, A. B. Schofield, D. Marenduzzo and W. C. K. Poon. *Science* **334**, 79-83 (2011).
10. U. Tkalec, M. Škarabot and I. Muševič. *Soft Matter* **4**, 2402 (2008).

11. A. Martinez, T. Lee, T. Asavei, H. Rubinsztein-Dunlop and I. I. Smalyukh. *Soft Matter* **8**, 2432 (2012).
12. B. Senyuk and I. Smalyukh. *Soft Matter* **8**, 8729 (2012).
13. J. Dontabhaktuni, M. Ravnik and S. Žumer. *Soft Matter* **8**, 1657 (2012).
14. G. M. Koenig, Jr., J. J. de Pablo, and N. L. Abbott, Langmuir **25**, 13318 (2009).
15. P. M. Phillips and A. D. Rey, Soft Matter **7**, 2052 (2011).
16. G. M. Koenig, Jr., R. Ong, A. D. Cortes, J. A. Moreno-Razo, J. J. de Pablo, and N. L. Abbott, Nano Lett. **9**, 2794 (2009).
17. M. Škarabot and I. Muševič, Soft Matter **6**, 5476 (2008).
18. B. Senyuk, J. S. Evans, P. J. Ackerman, T. Lee, P. Manna, L. Vigderman, E. R. Zubarev, J. van de Lagemaat, and I. I. Smalyukh, Nano Lett. **12**, 955 (2012).
19. P. Poulin and D. A. Weitz. *Phys. Rev. E* **57**, 626–637 (1998).
20. C. P. Lapointe, S. Hopkins, T. G. Mason and I. I. Smalyukh. *Phys. Rev. Lett.* **105**, 178301 (2010).
21. A. Martinez, H. C. Mireles and I. I. Smalyukh. *Procs. Natl. Acad. Sci. U.S.A.* **108**, 20891 (2011).
22. I. I. Smalyukh, J. Butler, J. D. Shrout, M. R. Parsek and G. C. L. Wong. Phys. Rev. E **78**, 030701 (2008).
23. O. D. Lavrentovich. *Curr. Opin. Colloid Interface Sci.* **21**, 97 (2016).
24. J. A. Moreno-Razo, E. J. Sambriski, G. M. Koenig, E. Díaz-Herrera, N. L. Abbott and J. J. de Pablo. *Soft Matter* **7**, 6828 (2011).
25. D. Abras, G. Pranami and N. L. Abbott. *Soft Matter* **8**, 2026 (2012).
26. U. M. Ognysta, A. B. Nych, V. A. Uzunova, V. M. Pergamenschik, V. G. Nazarenko, M. Škarabot and I. Muševič. *Phys. Rev. E* **83**, 041709 (2011).
27. M.B. Pandey, P.J. Ackerman, A. Burkart, T. Porenta, S. Žumer and I. I. Smalyukh. *Phys Rev E* **91**, 012501 (2015).
28. B. Senyuk, O. Puls, O. Tovkach, S. Chernyshuk and I. I. Smalyukh. *Nature Communications* **7**, 10659 (2016).
29. G. Scalia and J. Lagerwall (eds.). Liquid Crystals with Nano- and Microparticles. (World Scientific, 2016).
30. R. P. Trivedi, I. I. Klevets, B. Senyuk, T. Lee and I. I. Smalyukh. *Proc. Natl. Acad. Sci. U. S. A.* **109**, 4744 (2012).

31. V.S.R. Jampani, M. Škarabot, M. Ravnik, S. Čopar, S. Žumer and I. Muševič. *Phys. Rev. E* **84**, 031703 (2011).
32. J.S. Lintuvuori, K. Stratford, M.E. Cates and D. Marenduzzo. *Phys. Rev. Lett.* **107**, 267802 (2011).
33. Q. Liu, B. Senyuk, J. Tang, T. Lee, J. Qian, S. He and I. I. Smalyukh, *Phys. Rev. Lett.* **109**, 088301 (2012).
34. J.S. Lintuvuori, A.C. Pawsey, K. Stratford, M.E. Cates and P.S. Clegg. *Phys. Rev. Lett.* **110**, 187801 (2013).
35. F.B. MacKay and C. Denniston. *Europhys. Lett.* **94**, 66003 (2011).
36. M. Ravnik, M. Škarabot, S. Žumer, U. Tkalec, I. Poberaj, D. Babic, N. Osterman and I. Muševič. *Phys. Rev. Lett.* **99**, 247801 (2007).
37. J. S. Evans, Y. Sun, B. Senyuk, P. Keller, V. M. Pergamenshchik, T. Lee and I.I. Smalyukh. *Phys. Rev. Lett.* **110**, 187802 (2013).
38. M. Ravnik, G.P. Alexander, J.M. Yeomans and S. Žumer. *Faraday Discuss.* **144**, 159–169 (2010).
39. K. Stratford, O. Henrich, J.S. Lintuvuori, M.E. Cates and D. Marenduzzo. *Nat. Commun.* **5**, 3954 (2014).
40. K. Stratford, A. Gray and J. S. Lintuvuori. *J. Stat. Phys.* **161**, 1496-1507 (2015).
41. R. P. Trivedi, T. Lee, K. Bertness and I. I. Smalyukh. *Opt. Express* **18**, 27658 (2010).
42. M. C. M. Varney, Q. Zhang and I. I. Smalyukh. *Phys Rev E* **91**, 052503 (2015).
43. M. C. M. Varney, N. Jenness and I. I. Smalyukh. *Phys Rev E* **89**, 022505 (2014).
44. B. Senyuk, M. C. M. Varney, J. A. Lopez, S. Wang, N. Wu and I. I. Smalyukh. *Soft Matter* **10**, 6014 (2014).
45. D. Engström, M. C. M. Varney, M. Persson, R. P. Trivedi, K. A. Bertness, M. Goksör and I. I. Smalyukh. *Opt. Express* **20**, 7741 (2012).
46. R. P. Trivedi, D. Engström and I. I. Smalyukh. *J. Opt.* **13**, 044001 (2011).
47. I. Muševič. *Liq. Cryst. Today* **9**, 2-12 (2010).
48. T. Lee, R. P. Trivedi and I. I. Smalyukh. *Opt. Lett.* **35**, 3447 (2010).
49. P. M. Chaikin and T. C. Lubensky, *Principles of Condensed Matter Physics* (Cambridge University Press: Cambridge, 1995).
50. H. Stark. *Phys. Rep.* **351**, 387-474 (2001).
51. V. N. Manoharan. *Science* **349**, 1253751 (2015).

52. V. J. Anderson and H. N. W. Lekkerkerker. *Nature* **416**, 811-815 (2002).

53. S. Sacanna, W. T. M. Irvine, P. M. Chaikin and D. J. Pine. *Nature* **464**, 575-578 (2010).

54. Q. Liu, Y. Yuan and I. I. Smalyukh. *Nano Lett.* **14**, 4071-4077 (2014).

55. P. G. de Gennes and J. Prost, The Physics of Liquid Crystals, 2nd ed. (Clarendon, Oxford, 1993).

56. P. Oswald and P. Pieranski, Nematic and Cholesteric Liquid Crystals: Concepts and Physical Properties Illustrated by Experiments (Taylor & Francis/CRC Press, Boca Raton, FL, 2005).

57. S. Kralj, S. Žumer and D. W. Allender. *Phys. Rev. A* **43**, 2943–2952 (1991).

58. S. Chandrasekhar, *Liquid Crystals*, (Cambridge University Press: Cambridge, 2nd edn, 1992).

59. T. C. Lubensky, D. Pettey, N. Currier and H. Stark. *Phys. Rev. E* **57**, 610 (1998).

60. GNU Triangulated Surface Library (2006). Available at http://gts.sourceforge.net.

61. H. Si. TetGen, a Delaunay-Based Quality Tetrahedral Mesh Generator. *ACM Trans. Math. Softw.* **41**, 11 (2015).

62. R. Cools. An encyclopaedia of cubature formulas. *J. Complexity* **19**, 445–453 (2003).

63. P. Keast. *Comput. Methods Appl. Mech. Eng*. **55**, 339-348 (1986).

64. A. H. Stroud, *Approximate calculation of multiple integrals* (Prentice-Hall, Englewood Cliffs, N.J., 1971).

65. J. C. Gilbert and C. Lemaréchal. *Math. Program.* **45**, 407-436 (1989).

66. M. Tasinkevych, N. M. Silvestre and M. M. Telo da Gama. *New J. Phys*. **14**, 073030 (2012).

67. X. Wang, Y.-K. Kim, E. Bukusoglu, B. Zhang, D. S. Miller, and N. L. Abbott. *Phys Rev Lett* **116**, 147801 (2016).

68. H. Mori and H.Nakanishi, *J. Phys. Soc. Jpn.* **57**, 1281-1286 (1988).

69. E. M. Terentjev, *Phys. Rev. E* **51**, 1330-1337 (1995).

70. Z. Bradac□, S. Kralj, M. Svetec, and S. Z□umer, *Phys. Rev. E* **67**, 050702 (2003).

71. M. Svetec, S. Kralj, Z. Bradac□, and S. Z□umer, *Eur. Phys. J. E* **20**, 71-79 (2006).

72. J. C. Loudet, P. Barois, P. Auroy, P. Keller, H. Richard and P. Poulin. *Langmuir* **20**, 11336-11347 (2004).

73. U. Tkalec, M. Ravnik, S. Čopar, S. Žumer and I. Muševič. *Science* **333**, 62-65 (2011).